

Abell 48 - a rare WN-type central star of a planetary nebula^{*}

H. Todt^{1†}, A. Y. Kniazev^{2,3,4}, V. V. Gvaramadze^{4,5}, W.-R. Hamann¹,
D. Buckley³, L. Crause², S. M. Crawford^{2,3}, A. A. S. Gulbis^{2,3}, C. Hettlage^{2,3},
E. Hooper⁶, T.-O. Husser⁷, P. Kotze^{2,3}, N. Loaring^{2,3}, K. H. Nordsieck⁶,
D. O'Donoghue³, T. Pickering^{2,3}, S. Potter², E. Romero-Colmenero^{2,3},
P. Vaisanen^{2,3}, T. Williams⁸, M. Wolf⁶

¹University of Potsdam, Institute of Physics and Astronomy, 14476 Potsdam, Germany

²South African Astronomical Observatory, PO Box 9, 7935 Observatory, Cape Town, South Africa

³Southern African Large Telescope Foundation, PO Box 9, 7935 Observatory, Cape Town, South Africa

⁴Sternberg Astronomical Institute, Lomonosov Moscow State University, Moscow, Russia

⁵Isaac Newton Institute of Chile, Moscow Branch, Russia

⁶Department of Astronomy, University of Wisconsin-Madison, 475 N. Charter St., Madison, WI 53706, USA

⁷Institut für Astrophysik Georg-August-Universität, Friedrich-Hund-Platz 1, 37077 Göttingen, Germany

⁸Department of Physics and Astronomy, Rutgers University, 136 Frelinghuysen Road, Piscataway, NJ 08854, USA

Version from 2 December 2024

ABSTRACT

A considerable fraction of the central stars of planetary nebulae (CSPNe) are hydrogen-deficient. Almost all of these H-deficient central stars (CSs) display spectra with strong carbon and helium lines. Most of them exhibit emission line spectra resembling those of massive WC stars. Therefore these stars are classed as CSPNe of spectral type [WC]. Recently, quantitative spectral analysis of two emission-line CSs, PB 8 and IC 4663, revealed that these stars do not belong to the [WC] class. Instead PB 8 has been classified as [WN/WC] type and IC 4663 as [WN] type. In this work we report the spectroscopic identification of another rare [WN] star, the CS of Abell 48. We performed a spectral analysis of Abell 48 with the Potsdam Wolf-Rayet (PoWR) models for expanding atmospheres. We find that the expanding atmosphere of Abell 48 is mainly composed of helium (85 per cent by mass), hydrogen (10 per cent), and nitrogen (5 per cent). The residual hydrogen and the enhanced nitrogen abundance make this object different from the other [WN] star IC 4663. We discuss the possible origin of this atmospheric composition.

Key words: stars: abundances stars: AGB and post-AGB stars: mass-loss stars: Wolf Rayet planetary nebulae: general planetary nebulae: individual: PN G029.0+00.4

1 INTRODUCTION

During their evolution, low mass stars in a certain mass range become central stars of planetary nebulae (CSPNe). Central stars (CSs) are post-AGB stars with effective temperatures above 25 kK, hot enough to ionize circum-stellar material, which was shed off during the AGB phase. The ionized circum-stellar gas becomes visible in the optical as

a planetary nebula (PN) around the CS. While most of the low mass stars stay hydrogen-rich at the surface throughout their life, a fraction of about 20 per cent of CSs show a hydrogen-deficient surface composition. Almost all of these H-deficient CSs exhibit spectra with strong carbon and helium lines, indicating that their surface is composed predominantly by these elements (e.g. Górny & Tylenda 2000; Werner & Heber 1991).

About half of the H-deficient CSs show emission line spectra resembling those of massive WC stars, i.e. carbon-rich Wolf-Rayet (WR) stars with strong stellar winds. In analogy, the CSs with bright carbon emission lines are clas-

^{*} Based on observations obtained with the South African Large Telescope (SALT), commissioning programme 2010-1-RSA_OTH-001 and programme 2011-3-RSA_OTH-002.

† E-mail: htodt@astro.physik.uni-potsdam.de

sified as [WC] stars, where the brackets should distinguish them from their massive counterparts.

Recently, quantitative spectral analysis of two CSs with broad emission lines revealed that they do not belong to the [WC] class. The first one was PB 8 (Todt et al. 2010a), which should be classified as [WN/WC] type, and the other one was IC 4663 (Miszalski et al. 2012), which shows a [WN] type spectrum. In both cases the atmospheres of these stars are mainly composed of helium. The atmosphere of PB 8 also contains hydrogen and traces of carbon, nitrogen, and oxygen, while IC 4886 has an almost pure helium atmosphere with only traces of nitrogen.

For some other CSs the membership to the [WN] class was discussed, but could not be proven (Todt et al. 2010b). DePew et al. (2011) mentioned the CS of Abell 48, which shows a WN-type spectrum, but it was not clear whether this is really a CSPN and not a massive WN star with a ring nebula. In this paper, we present a quantitative analysis of the optical spectrum of the CS of Abell 48, which reveals indeed a WN-like atmospheric composition. We will also present arguments for the low-mass nature of Abell 48.

The paper is organized as follows: Section 2 gives an overview of previous observations of Abell 48. In Section 3 we describe our observations and the data reduction. A short description of our methods is given in Section 4. The spectral analysis is presented in Section 5. Section 6 deals with the nebula, while the results and implications are discussed in Section 7.

2 ABELL 48

Abell 48 was discovered by Abell (1955) on the original plates of the Palomar Sky Survey. In the red photograph from this survey (presented in fig. 1 in Abell 1966), Abell 48 appears as a slightly elliptical double-ringed nebula with a major axis diameter of about $40''$ (see also the left panel of Fig. 1 for the Digitized Sky Survey II (DSS-II) red band (McLean et al. 2000) image of the nebula). Abell (1955, 1966) classed the nebula as PN (listed in the discovery papers under numbers 36 and 48, and named in the SIMBAD database PN A55 36 and PN A66 48, respectively), while its CS has not been classified. Since that time, the PN classification of Abell 48 was generally accepted and the nebula was included in the Strasbourg-ESO Catalogue of Galactic Planetary Nebulae (Acker et al. 1992) under the name PN G029.0+00.4.

Abell 48 is a strong radio source. With the 1.4 GHz flux of 159 ± 15 mJy (Condon & Kaplan 1998), it is one of the brightest objects among the PNe covered by the NRAO VLA Sky Survey (NVSS; Condon et al. 1998). The circular shell of Abell 48 was clearly resolved in the Multi-Array Galactic Plane Imaging Survey (MAGPIS; Helfand et al. 2006), carried out with the Very Large Array (VLA)¹. In the MAGPIS 20 cm image Abell 48 appears as a thick shell of the same size as the optical nebula (see Fig. 1).

Abell 48 was also detected in several major mid- and far-infrared (IR) surveys, while its ring-like shell has been

Table 1. The central star of Abell 48.

RA(J2000)	18 ^h 42 ^m 46 ^s .91
Dec.(J2000)	−03°13′17″.2
<i>l</i>	29°0784
<i>b</i>	0°4543
<i>B</i> (mag)	19.40±0.35
<i>R</i> (mag)	16.67±0.34
<i>I</i> (mag)	15.50±0.05
<i>J</i> (mag)	13.51±0.03
<i>H</i> (mag)	12.83±0.03
<i>K_s</i> (mag)	12.33±0.03
[3.6] (mag)	11.69±0.06
[4.5] (mag)	11.25±0.10
[5.8] (mag)	11.06±0.09
[8.0] (mag)	11.04±0.16

resolved in the IR only with the advent of the *Spitzer Space Telescope* (Phillips & Ramos-Larios 2008; Wachter et al. 2010). Figure 1 includes the *Spitzer* 8 and $24\ \mu\text{m}$ images of Abell 48 obtained with the Infrared Array Camera (IRAC; Fazio et al. 2004) and the Multiband Imaging Photometer for *Spitzer* (MIPS; Rieke et al. 2004) within the framework of the Galactic Legacy Infrared Mid-Plane Survey Extraordinaire (GLIMPSE; Benjamin et al. 2003) and the 24 and 70 Micron Survey of the Inner Galactic Disk with MIPS (MIPSGAL; Carey et al. 2009), respectively. In the $8\ \mu\text{m}$ image the nebula shows a bright inner shell and a diffuse outer halo with an angular extent equal to that of the outer optical shell, while at $24\ \mu\text{m}$ its morphology is very similar to that of the radio nebula.

To our knowledge, there was not any significant study of Abell 48 until recently. The interest in Abell 48 has arisen after Wachter et al. (2010) carried out optical spectroscopy of its CS and classified it as WN6. Based on this result, DePew et al. (2011) and Bojicic et al. (2012) have speculated that Abell 48 might be another member of the [WN] or [WN/WC] class (Todt et al. 2010a), but there has not been a detailed study yet.

Table 1 gives the coordinates and photometry of the CS of Abell 48. The *B* and *R* magnitudes are from the Guide Star Catalogue (GSC2.2)², the *I* magnitude is from the DENIS (Deep Near Infrared Survey of the Southern Sky) database (DENIS Consortium 2005), the *J*, *H*, *K_s* magnitudes are from the 2MASS (Two Micron All Sky Survey) All-Sky Catalog of Point Sources (Cutri et al. 2003), and the coordinates and the IRAC magnitudes are from the GLIMPSE Source Catalog (*I* + *II* + 3D)³.

3 OBSERVATIONS AND DATA REDUCTION

Abell 48 was observed within the framework of our ongoing programme of spectroscopic follow-up observations dedicated to evolved massive star candidates that were revealed through the detection of their IR circumstellar nebulae (Gvaramadze et al. 2009, 2010a,b,c, 2011, 2012; Stringfellow et al. 2011, 2012). Although Abell 48 was not included in our (Gvaramadze et al. 2010a) list of compact nebulae

¹ The authors of this survey classed Abell 48 as a high-probability supernova remnant candidate.

² <http://vizier.u-strasbg.fr/viz-bin/VizieR?-source=I/271>

³ <http://cdsarc.u-strasbg.fr/viz-bin/Cat?II/293>

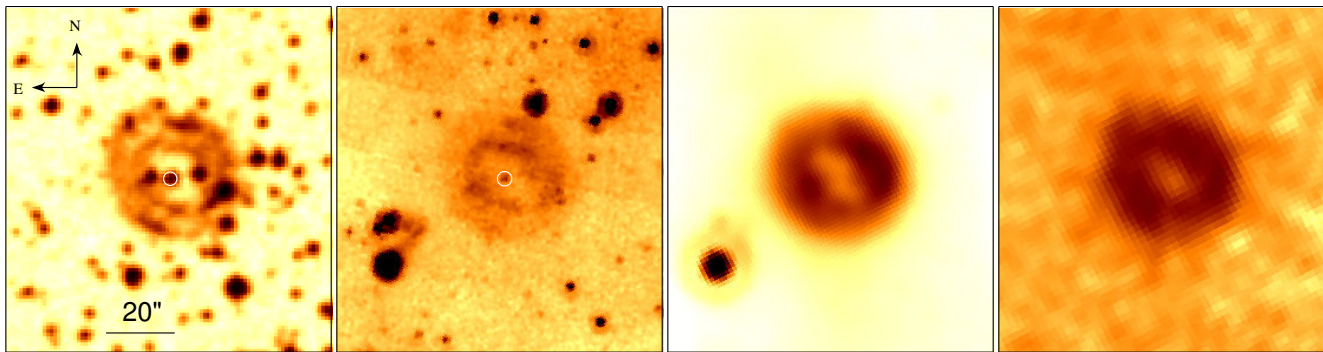


Figure 1. From left to right: DSS-II red band, *Spitzer* 8 and 24 μm , and the VLA 20 cm images of Abell 48 and its central star (marked by a circle in the DSS-II and 8 μm images). The orientation and the scale of the images are the same.

with central stars (because it was identified in the SIMBAD database as a PN), we decided to observe it to check whether its CS is an ordinary WN star (as suggested by Wachter et al. 2010) or we deal with an extremely rare object – a [WN]-type CSPN.

Spectral observations of Abell 48 were obtained with the Southern African Large Telescope (SALT; Buckley et al. 2006; O’Donoghue & et al. 2006) on 2011 August 25 during the Performance Verification phase of the Robert Stobie Spectrograph (RSS; Burgh et al. 2003; Kobulnicky et al. 2003), and one more spectrum was taken on 2012 April 12. The long-slit spectroscopy mode of the RSS was used, with a slit width of $1''.25$ and a position angle of 0° for all observations. The seeing was stable in the range of $1''.6$ to $2''.0$. We utilized a binning factor of 2, to give a final spatial sampling of $0''.258 \text{ pixel}^{-1}$. The Volume Phase Holographic (VPH) grating GR900 was used in these observations to cover a total spectral range of $4300\text{--}7300 \text{ \AA}$ with a final reciprocal dispersion of $\sim 0.97 \text{ \AA pixel}^{-1}$ and a spectral resolution FWHM of $5\text{--}6 \text{ \AA}$. Three exposures were taken, each with 15 minutes. Spectra of the Xe comparison arc were obtained to calibrate the wavelength scale. Spectrophotometric standard stars were observed during twilight.

RSS has three mosaiced 2048×4096 CCDs as a detector. First, data for each CCD were overscan subtracted, trimmed, gain and cross-talk corrected, and finally mosaiced. This primary data reduction was done with the SALT science pipeline (Crawford et al. 2010). Second, primary corrected and mosaiced long-slit data were reduced in the way described in Kniazev et al. (2008b). Finally, all two-dimensional spectra were averaged. The spectrum of the surrounding nebula was subtracted using the IRAF **background** task and a one-dimensional spectrum of the CS was extracted with the **apall** task. The two-dimensional spectrum of the surrounding nebula was averaged along the slit.

SALT is a telescope with a variable pupil, and its illuminating beam changes continuously during the observation. This makes an absolute flux calibration impossible, even using spectrophotometric standard stars or photometric standards. Therefore the spectrophotometric standard stars were used only for a relative flux calibration, and the absolute flux level was scaled to the photometric R magnitude.

4 METHODS

4.1 Spectral modelling

For the analysis of the spectrum we used the Potsdam Wolf-Rayet (PoWR) models for expanding atmospheres (see Gräfener et al. 2002; Hamann & Gräfener 2004). The PoWR code solves the non-LTE radiative transfer problem in a spherically expanding atmosphere simultaneously with the statistical equilibrium equations while accounting for energy conservation. Iron-group line blanketing is treated by means of the superlevel approach. Wind inhomogeneities in first-order approximation are taken into account, assuming small-scale clumps. In this work, we do not calculate hydrodynamically self-consistent models, as in Gräfener & Hamann (2005), but assume that the velocity field follows a β -law with $\beta = 1$ with the mass-loss rate as a free parameter. Our computations include complex atomic models for hydrogen, helium, carbon, nitrogen, oxygen, and the iron-group elements. Within our group, this code has been extensively used for quantitative spectral analyses of massive WR stars (e.g. Gräfener et al. 2002; Liermann et al. 2010) and WR-type CSPN (e.g. Todt et al. 2010a).

4.2 Spectral fitting

The typical emission-line spectra of Wolf-Rayet stars are predominantly formed by recombination processes in their dense stellar winds. Therefore the continuum-normalized spectrum shows a useful scale-invariance: for a given stellar temperature T_* and chemical composition, the equivalent widths of the emission lines depend only on the ratio between the volume emission measure of the wind and the area of the stellar surface, to a first approximation. An equivalent quantity, introduced by Schmutz, Hamann, & Wessolowski (1989), is the *transformed radius*

$$R_t = R_* \left[\frac{v_\infty}{2500 \text{ km s}^{-1}} / \frac{\dot{M}\sqrt{D}}{10^{-4} \text{ M}_\odot \text{ yr}^{-1}} \right]^{2/3}. \quad (1)$$

Different combinations of stellar radii R_* and mass-loss rates \dot{M} can thus lead to nearly the same emission-line strengths. In the form given here, the invariance also includes the micro-clumping parameter D , which is defined as the density contrast between wind clumps and a smooth wind of the same mass-loss rate. Consequently, mass-loss rates derived

empirically from fitting the emission-line spectrum depend on the adopted value of D . The latter can be constrained by fitting the extended electron scattering wings of strong emission lines (e.g. Hillier 1991; Hamann & Koesterke 1998).

5 ANALYSIS

5.1 Stellar parameters

In order to find the model that best matches to the observation, we choose a systematic approach: We begin with a first determination of $\log T_*$ and $\log R_t$ with the help of the already existing model grid for massive WN stars of the late subtypes (WNL)⁴ (Hamann & Gräfener 2004), which was recently updated with improved atomic data.

For each of the models in this grid, we calculated the reduced χ^2_ν

$$\chi^2_\nu = \frac{1}{N} \sum_{i=1}^N \frac{(f_i^{\text{obs}} - f_i^{\text{mod}})^2}{\sigma^2}. \quad (2)$$

f^{obs} denotes the by-eye rectified observed spectrum and f^{mod} the continuum normalized synthetic spectrum of the model, each with N data points. We consider R_t and T_* as the fitting parameters. We adjusted the uncertainty σ so, that the reduced χ^2_ν of the best fitting model equals unity, corresponding to a mean deviation of about 20 per cent. The best fitting model is the one with $\log T_*/\text{K} = 4.85$ and $\log R_t/R_\odot = 0.9$ [...].

The models of this grid had been calculated with a bolometric luminosity of $\log L/L_\odot = 5.3$ and a density contrast of $D = 4$, as appropriate for many massive WN stars (Hamann et al. 2006). However, in Section 7 we present arguments that Abell 48 is in fact a PN. Therefore we calculated a grid of models with parameters that are more appropriate for CSPNe, i.e. for the stellar luminosity and mass of $L = 6000 L_\odot$ and $M = 0.6 M_\odot$ (see e.g. Schönberner et al. 2005; Miller Bertolami & Althaus 2007).

Moreover, with our first estimate of R_t and T_* we calculated a series of models with different chemical abundances to determine the most appropriate atmospheric composition. The best fit is achieved with the abundances presented in Table 3, as described in Section 5.2. These abundances were used for our [WN] grid.

Since there is no UV observation available that would contain spectral lines with P Cygni profiles, we had to deduce the wind terminal velocity, v_∞ from the width of the optical emission lines. The best fit is achieved with $v_\infty = 1000 \pm 200 \text{ km s}^{-1}$. Line broadening by microturbulence is also included in our models. From the shape of the line profiles we estimated the microturbulence to be about 100 km s^{-1} .

We repeated our χ^2_ν -fit analysis for this grid of [WN] models to get the uncertainties in R_t and T_* (see Fig. 2). The 1σ -uncertainties can be obtained from the contour with $\chi^2_\nu = 2$, i.e. where the value of χ^2_ν has increased by 1 compared to the best-fitting model, for which $\chi^2_\nu = 1$. The best-fitting model from this [WN] grid, has $T_* = 71^{+12}_{-9} \text{ kK}$ and

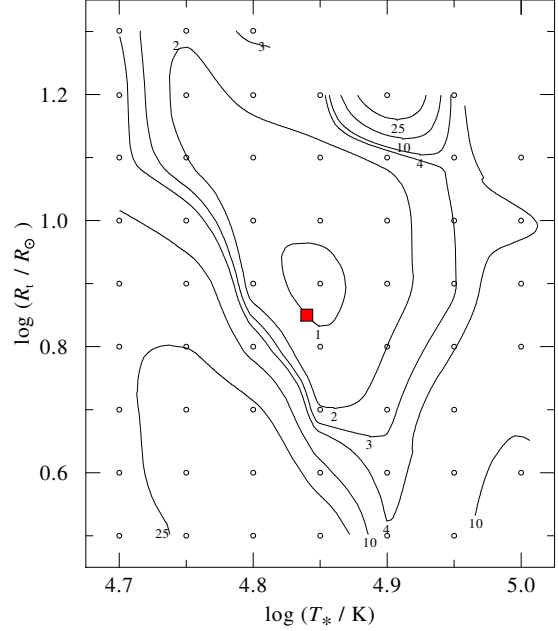


Figure 2. Contours of the reduced χ^2_ν for our grid of [WN] models. The open circles indicate the calculated models. Between these data points the contour lines are interpolated. Note that a $\Delta\chi^2_\nu = 1$ corresponds to a 1σ confidence interval. Thus, the contour with $\chi^2_\nu = 2$ indicates the 1σ uncertainty of the parameters R_t and T_* . Our final model is indicated by the red square.

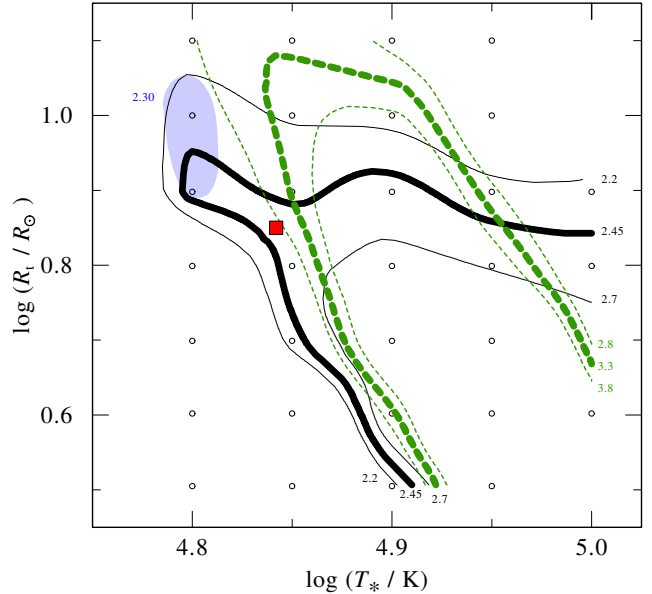


Figure 3. Contours of the ratio between the line peak heights of N IV 7100 / N III 4643 (green dashed lines), N IV 7100 / N V 4933 (blue filled ellipse), and He II 5412 / He I 5876 (black solid lines). The thick contours represent the measured values, the thinner lines the 1σ uncertainty. The other symbols are the same as in Fig. 2.

⁴ <http://www.astro.physik.uni-potsdam.de>

Table 2. Ratios between the peak heights: measured ratios, inferred quantities, and ratios from the final model.

Line ratio	Observed	Final model
He II λ 5412 / He I λ 5876	2.45 ± 0.25	2.2
N IV λ 7120 / N III λ 4634	3.3 ± 0.5	2.3
N IV λ 7120 / N V λ 4933/43	2.8 ± 0.3	2.1

$\log R_t/R_\odot = 0.9 \pm 0.2$, where the given error margin corresponds to a doubling of the deviation between model and observation, as measured by the reduced χ^2_ν (see Equation 2).

For a further refinement, we calculated the line-strength ratios between significant lines of He II / He I, N IV / N III, and N IV / N V for this grid and compared them to the observation (cf. Table 2). We used line ratios instead of absolute line strengths to diminish the influence of chemical abundances. In practice, it is often difficult to measure the equivalent widths of lines correctly, e.g. due to line blends. Therefore we used the peak height as a measure of the line strength.

From our optical observation we estimate the uncertainty in the normalized continuum to be of the order of 10 per cent in the region of the N III λ 4643 line and 5 per cent at the other diagnostic lines. We consider this as the uncertainty in the peak measurement, which we then use to infer a 10 per cent uncertainty in the measured He II / He I and N IV / N V peak height ratio and a 15 per cent uncertainty in the measured N IV / N III peak height ratio.

In Figure 3 we show contours of the N IV / N III and He II / He I line peak ratios. The bold lines correspond to the observed values. These contours have two intersections. As a further criterion we now consider the N IV / N V ratio. Unfortunately, all models of the grid give a smaller value than observed, but the two models encircled by the shaded area in the upper left corner of the diagram come closest. After manual inspection of the spectral fits we finally decided for the final model with $\log R_t/R_\odot = 0.85^{+0.15}_{-0.13}$ and $T_* = 70^{+4}_{-5}$ kK, indicated by the red square in Figure 3. The given uncertainties were estimated from the 1σ contours in this figure.

Remarkably, the final parameters derived under assumption of a CS luminosity hardly differ from those obtained above from the massive star grid. This demonstrates that the scale-invariance for models with same R_t holds over a wide parameter range.

Together with the normalized spectrum we obtained the synthetic spectral energy distribution (SED) in absolute units from the PoWR models. The synthetic SED was fitted to the flux-calibrated spectrum and photometric measurements by adjusting the distance and the reddening parameter E_{B-V} (cf. Fig. 5). The photometric magnitudes for the Johnson and 2MASS measurements were converted to fluxes with help of the calibrations by Holberg & Bergeron (2006), the IRAC measurements with help of the calibrations by Cohen et al. (2003).

The best SED-fit was obtained with a color excess of $E_{B-V} = 2.10$ mag and the standard total-to-selective absorption ratio $R_V = 3.1$ (Fitzpatrick 1999). We estimated a distance of $d = 1.9$ kpc towards Abell 48 with the adopted stellar luminosity of $6000 L_\odot$.

5.2 Element abundances

In an iterative process with the determination of T_* and R_t , we varied the abundances of He, H, C, N, and O. As there is no UV-spectrum of the CS of Abell 48 available that would help to determine the abundances of the iron-group elements, we kept latter fixed to solar values.

Helium. From the strengths of the helium emission lines, especially He II 4-3, it is already obvious that the wind is mostly composed of helium.

Hydrogen. None of our models is able to reproduce the H α /He II and H β /He II blends together with the unblended He II 7-4 line simultaneously as observed (cf. Fig. 6). H β fits best with a hydrogen mass fraction of 20 per cent, while the H α /He II blend matches the observation with about 3 per cent of hydrogen. As a compromise we adopt a value of 10 per cent of hydrogen. A better resolved spectrum with a higher signal-to-noise ratio (S/N) would help to pin down the exact hydrogen abundance.

Nitrogen. The nitrogen lines in the spectrum of the CS of Abell 48 are much stronger than in WN spectra of stars with similar parameters. We had to increase the nitrogen abundance to 5 per cent by mass to match the observed line strength of the N V λ 4933/4944 multiplet and most of the other nitrogen lines. The N IV λ 7125 line and the N IV/N V blend at 4600 Å are unfortunately not well matched by our model. Models with only $X_N = 3$ per cent provide a much better fit to the N III λ 4634 line, while the strength of the N IV λ 7125 line is best reproduced by models with $X_N = 7$ per cent. Generally, it is hard to find a sufficient fit for spectral lines of three different ions from the same element. This might be an indication for an inhomogeneous wind.

Carbon. In the absence of other carbon lines within the range of our observed spectrum we have to rely on the C IV λ 5800 line only. This line can be best fitted with a model that has a carbon abundance of 0.3 per cent by mass. The given uncertainty of ± 0.1 per cent accounts only for the uncertainty of the continuum normalization.

Oxygen. There are no strong oxygen lines in the spectral range of our observation. A model with solar oxygen abundance of $X_O = 0.6$ per cent by mass predicts a weak emission line from O III λ 5592 with a line strength that is almost below the detection limit. A higher oxygen abundance would not be compatible with the observation.

The final line fit is shown in Fig. 4 and the model parameters are compiled in Table 3.

6 THE NEBULA OF ABELL 48

6.1 Position-velocity diagram along the slit

In Fig. 7 we present the H α intensity and radial velocity distributions along the slit, and the DSS-II red band image of Abell 48 for comparison. The extension of the nebula in the H α line is very similar to that in the DSS-II image. H α emission appears everywhere within the nebula and its peaks are clearly correlated with the CS and the shell's position. We measured the diameter of the nebula of $43''$ at a ten per cent level of the peak intensity in the H α line. At the distance of Abell 48 of 1.9 kpc (see Sections 5.1 and 7.3) the radius of the nebula is about 0.2 pc.

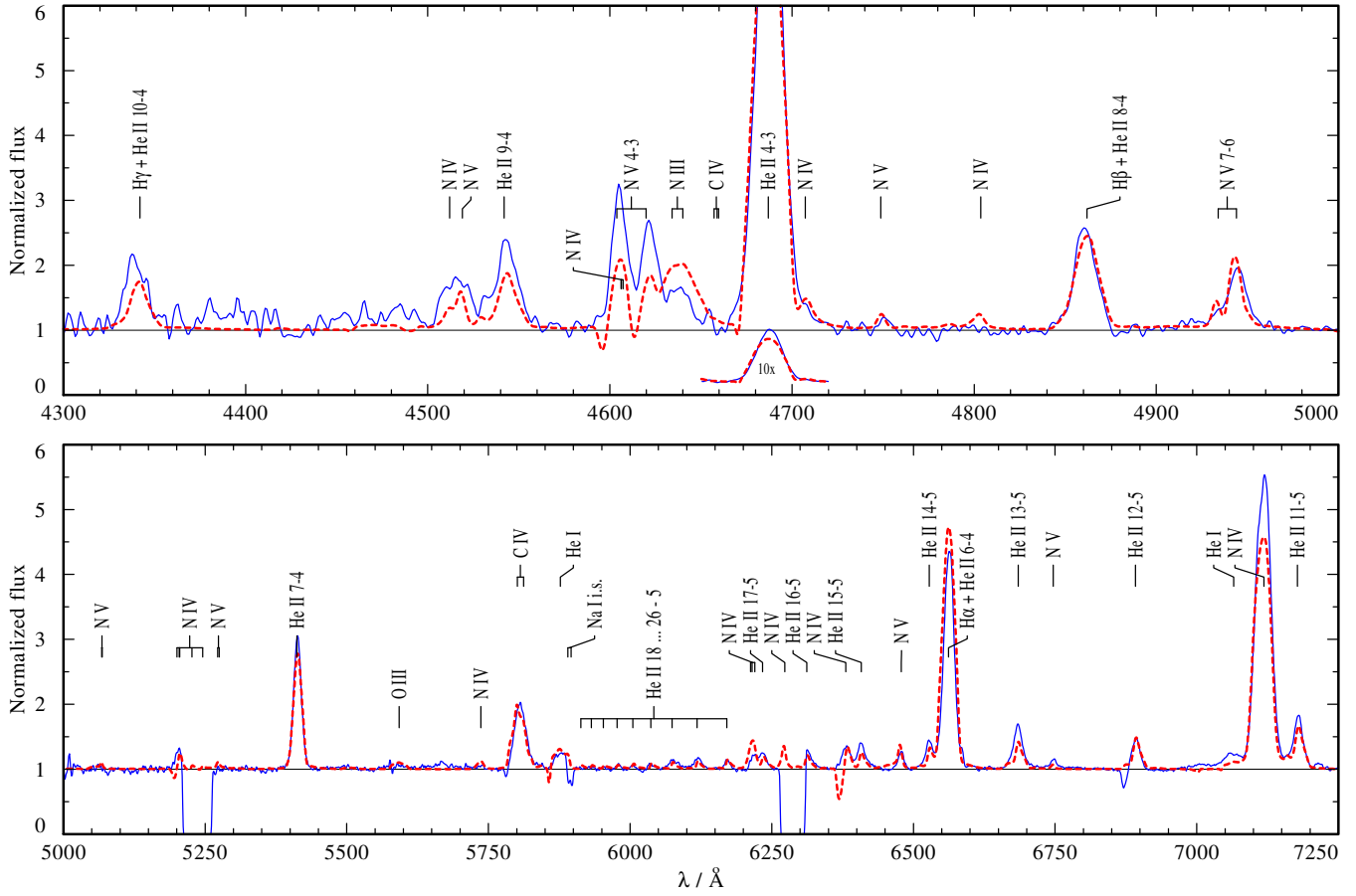


Figure 4. Optical spectrum of the CS of Abell 48: Observation (blue solid) vs. synthetic spectrum (red dashed). The observed spectrum has some gaps and gets much noisier towards shorter wavelengths.

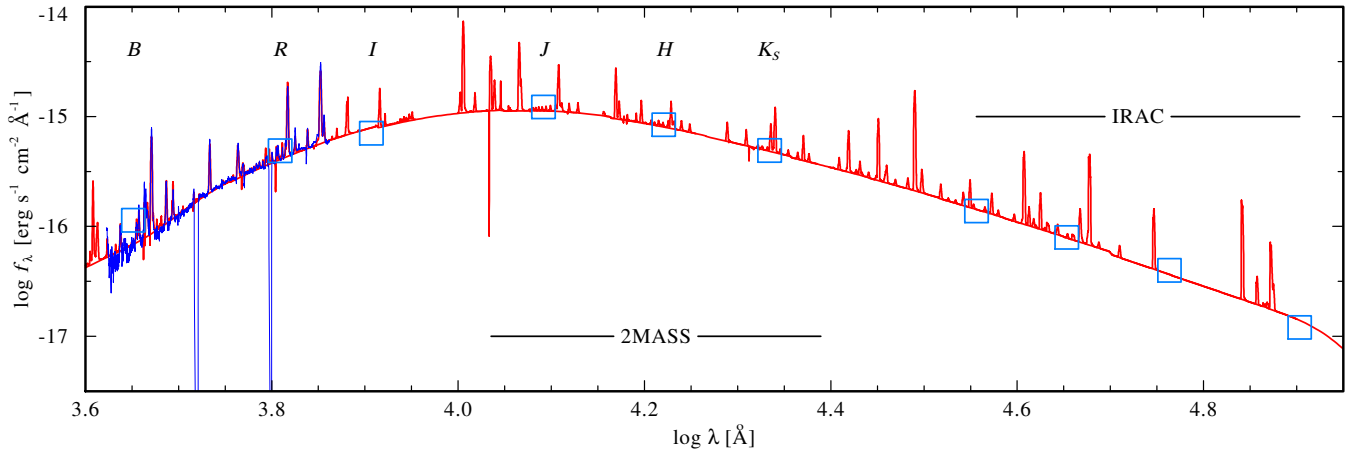


Figure 5. Observed flux distribution of Abell 48 (blue/noisy) in absolute units, including the calibrated spectrum and the photometric measurements (open blue squares, see Table 1), compared to the emergent flux of the model (red/smooth line). The model flux has been reddened and scaled to the distance according to the parameters given in Table 3.

We calculated the line-of-sight velocity distribution (v_{hel}) along the slit using the method and programs described in Zasov et al. (2000). To exclude systematic shifts originating from the known RSS flexure, the closest bright night sky line [O I] $\lambda 6363 \text{ \AA}$ was used. Finally, only those

velocity estimates were used which satisfy the criteria $S/N > 3$ and $\sigma_v < 10 \text{ km s}^{-1}$.

Fig. 7 shows that v_{hel} along the slit spans a range of ≈ 0 to 50 km s^{-1} . This range is very similar to that found for PNe (see e.g., Torres-Peimbert et al. 2009). We measured $v_{\text{hel}} = 50.4 \pm 4.2 \text{ km s}^{-1}$ in the area which is closest to the position

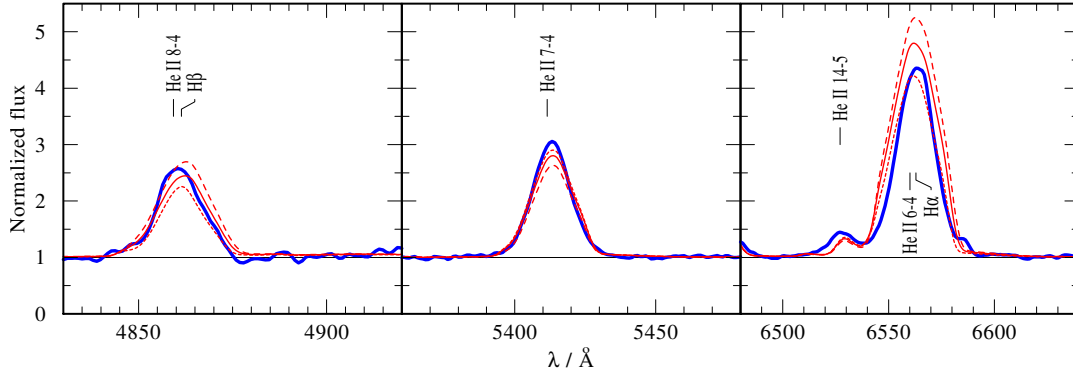


Figure 6. Test for the hydrogen abundance in the CS of Abell 48. The observed profiles (blue/thick solid line) are compared with models (red/thin lines) for different hydrogen abundance, but otherwise the same parameters as of our best-fit model (see Table 3). The tested hydrogen mass fractions are zero (dotted lines), 10 per cent (thin solid lines) and 20 per cent (dashed lines), respectively.

Table 3. Abell 48: Stellar and wind parameters.

T_*	70^{+4}_{-5}	kK
v_∞	1000 ± 200	km s $^{-1}$
$\log R_t$	$0.85^{+0.15}_{-0.13}$	R_\odot
$\log \dot{M}$	-6.4 ± 0.2	M_\odot yr $^{-1}$
R_*	0.54 ± 0.07	R_\odot
D	4	(density contrast)
E_{B-V}	2.10 ± 0.05	mag
v_{rad}	50 ± 4	km s $^{-1}$
H	10 ± 10	per cent by mass
He	85 ± 10	per cent by mass
C	0.3 ± 0.1	per cent by mass
N	5.0 ± 2.0	per cent by mass
O	≤ 0.6	per cent by mass
Fe	1.4×10^{-3}	per cent by mass

of the CS and suggest that this velocity corresponds to the velocity of the mass center. With our spectral resolution ($\text{FWHM} = 5.5 \pm 0.5 \text{ \AA}$) for the range of the $\text{H}\alpha$ line, we are not able to measure the expansion velocity directly.

6.2 Physical conditions and chemical abundances

The spectrum of the nebula of Abell 48 has never been studied before, because it is relatively faint and highly reddened. An objective prism spectrum was taken by Sanduleak (1976), where only the $\text{H}\alpha$ line was detected. DePew et al. (2011) studied the CS of Abell 48 with the Siding Spring Observatory 2.3m telescope, but they did not publish any spectrum. Even with SALT we were not able to detect any useful signal in the spectral range below 4300 \AA . Our final 1D spectrum of the nebula is shown in Fig. 8.

Emission lines [...] in the spectrum of the surrounding nebula were measured applying the MIDAS programs described in detail in Kniazev et al. (2004, 2005). Table 4 lists the measured relative intensities of all detected emission lines relative to $\text{H}\beta$ ($F(\lambda)/F(\text{H}\beta)$), the ratios corrected for the extinction ($I(\lambda)/I(\text{H}\beta)$), and the derived extinction coefficient $C(\text{H}\beta)$. The latter corresponds to E_{B-V} of 2.15 mag, which is very similar to the value found independently from the spectrum of the CS (see Table 3).

The spectrum of the nebula was interpreted by the tech-

Table 4. Line intensities of the nebula Abell 48.

$\lambda_0(\text{\AA})$ Ion	$F(\lambda)/F(\text{H}\beta)$	$I(\lambda)/I(\text{H}\beta)$
4340 $\text{H}\gamma$	0.170 ± 0.009	0.451 ± 0.024
4363 [O III]	0.014 ± 0.005	0.034 ± 0.013
4861 $\text{H}\beta$	1.000 ± 0.031	1.000 ± 0.033
4959 [O III]	1.187 ± 0.030	1.005 ± 0.026
5007 [O III]	4.050 ± 0.094	3.165 ± 0.077
5755 [N II]	0.018 ± 0.002	0.004 ± 0.001
5876 He I	0.974 ± 0.024	0.206 ± 0.005
6364 [O I]	0.042 ± 0.003	0.005 ± 0.000
6548 [N II]	3.103 ± 0.118	0.282 ± 0.012
6563 $\text{H}\alpha$	32.555 ± 0.721	2.906 ± 0.074
6584 [N II]	8.831 ± 0.215	0.770 ± 0.021
6678 He I	0.616 ± 0.015	0.048 ± 0.001
6717 [S II]	0.761 ± 0.018	0.057 ± 0.002
6731 [S II]	0.915 ± 0.021	0.068 ± 0.002
7065 He I	0.434 ± 0.012	0.022 ± 0.001
7136 [Ar III]	2.117 ± 0.051	0.102 ± 0.003
7237 [Ar IV]	0.057 ± 0.003	0.003 ± 0.000
7281 He I	0.170 ± 0.010	0.007 ± 0.000
7320 [O II]	0.174 ± 0.014	0.007 ± 0.001
7330 [O II]	0.156 ± 0.014	0.006 ± 0.001
$C(\text{H}\beta)$ dex	3.16 ± 0.03	
E_{B-V} mag	2.15 ± 0.01	

nique of plasma diagnostics in the way described in detail in Kniazev et al. (2008b). The electron temperatures $T_e(\text{O III})$, $T_e(\text{N II})$, were calculated directly using the weak auroral lines of oxygen [O III] $\lambda 4363$ and nitrogen [N II] $\lambda 5755$. Both temperatures and the number density $n_e(\text{S II})$ are given in Table 5. From the detected emission lines we were able to determine the total element abundances for O, N, Ar, and He. These results are shown in Table 5 together with solar abundances (Asplund et al. 2009).

The derived abundances of the α -elements O and Ar are lower than solar by about -0.3 dex. In contrast, He and N show abundances close to the solar values.

The IR fluxes at wavelengths longer than $8 \mu\text{m}$, which have been measured by *Midcourse Space Experiment* (MSX) satellite (Price et al. 2001) and the *Wide-field Infrared Survey Explorer* (WISE; Wright et al. 2010), show a strong excess compared to the predicted stellar continuum. This excess could be due to the low resolution of these instruments,

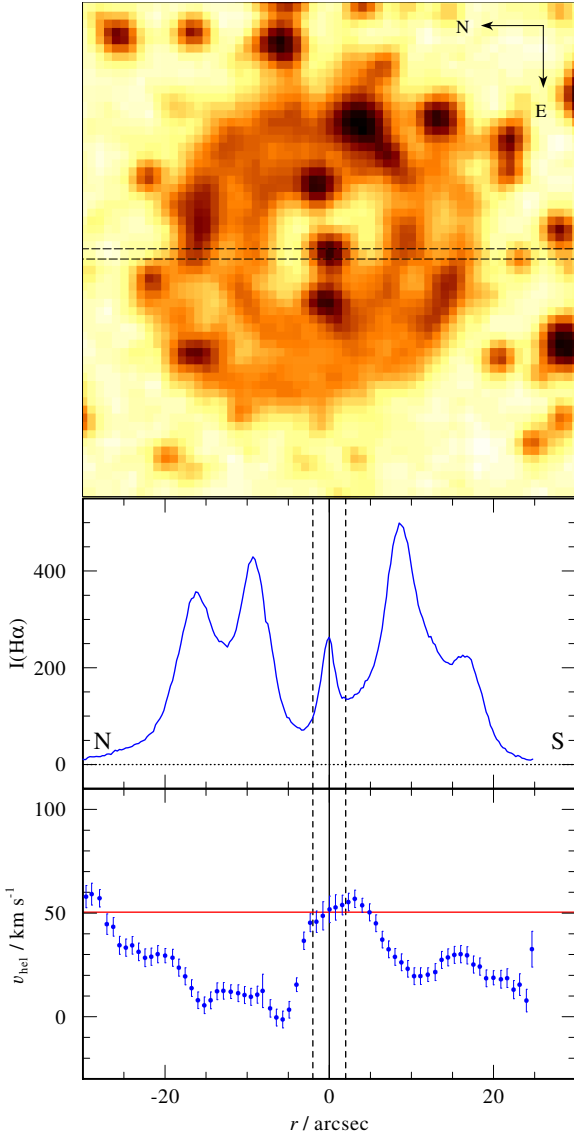


Figure 7. $H\alpha$ intensity and radial velocity distribution along the slit. *Upper panel:* DSS-II red band image of Abell 48 with the position of the $1''.25$ slit shown by dashed lines. *Middle panel:* The relative flux of the $H\alpha$ -line along the slit after continuum subtraction. N-S direction of the slit is shown. The vertical line at $r = 0$ corresponds to the position of the CS. The region $r \pm 2''$ is shown with vertical, dashed lines to mark the area, where the average velocity $v_{\text{hel}} = 50.4 \pm 4.2 \text{ km s}^{-1}$ was calculated. *Bottom panel:* The velocity profile of the $H\alpha$ line, corrected by using the night-sky line $[\text{O I}] \lambda 6363 \text{ \AA}$. The horizontal line indicates the calculated velocity 50.4 km s^{-1} , that has to be close to the heliocentric velocity of the CS.

which results in confusion between the stellar source and the nebular emission.

7 DISCUSSION

As discussed in the introduction, there were doubts whether Abell 48 is a PN with a low-mass central star or a ring nebula around a massive star. Now we discuss several arguments in favour of the PN status of this object.

Table 5. Elemental abundances in the nebula of Abell 48.

Quantity	Abell 48	Sun ^a
$T_e(\text{O III}) / \text{K}$	$11\,870 \pm 1\,640$	
$T_e(\text{N II}) / \text{K}$	$7\,200 \pm 750$	
$n_e(\text{S II}) / \text{cm}^{-3}$	$1\,000 \pm 130$	
$\text{O}^+ / \text{H}^+ (\times 10^5)$	19.97 ± 5.89	
$\text{O}^{++} / \text{H}^+ (\times 10^5)$	6.56 ± 2.74	
$\text{O} / \text{H} (\times 10^5)$	26.53 ± 6.49	
$12 + \log(\text{O} / \text{H})$	8.42 ± 0.11	8.69
$\text{N}^+ / \text{H}^+ (\times 10^7)$	416.9 ± 151.6	
$\text{ICF}(\text{N})$	1.55	
$\text{N} / \text{H} (\times 10^5)$	6.48 ± 2.36	
$12 + \log(\text{N} / \text{H})$	7.81 ± 0.16	7.83
$\log(\text{N} / \text{O})$	-0.61 ± 0.19	-0.86
$\text{Ar}^{++} / \text{H}^+ (\times 10^7)$	6.06 ± 2.53	
$\text{ICF}(\text{Ar})$	1.21	
$\text{Ar} / \text{H} (\times 10^7)$	7.33 ± 3.05	
$12 + \log(\text{Ar} / \text{H})$	5.86 ± 0.18	6.40
$\log(\text{Ar} / \text{O})$	-2.56 ± 0.21	-2.29
He / H	0.133 ± 0.005	
$12 + \log(\text{He} / \text{H})$	11.12 ± 0.02	10.93

^a Solar abundances from Asplund et al. (2009)

7.1 Abell 48 – a PN or a ring nebula around a massive WR star?

The analysis of the spectrum of the nebula of Abell 48 gives us indications that this object is most likely a PN, and not a nebula around a massive star:

Diagnostic diagrams are very often used to classify emission line sources and separate them from each other on the base of the most important line ratios (see e.g., Knizhev et al. 2008a; Frew & Parker 2010, and references therein). The most frequently used diagnostic diagram is $\log(F(\text{H}\alpha)/F([\text{N II}] \lambda\lambda 6548, 6584))$ versus $\log(F(\text{H}\alpha)/F([\text{S II}] \lambda\lambda 6717, 6731))$. For Abell 48 these ratios are 0.44 vs. 1.37. With these values, Abell 48 is located in the middle of the region occupied by PNe and far away from the place where H II regions and WR shells are typically found.

The density of the Abell 48 nebula and the diagnostic diagram $\log([\text{S II}] \lambda 6717/\lambda 6731)$ versus $\log(F(\text{H}\alpha)/F([\text{N II}] \lambda\lambda 6548, 6584))$ also puts this source into the region of PNe (cf. Figure 9), but not of WR shells, which all have densities similar to those of H II regions (Esteban et al. 1992, 1994; Garnett & Chu 1994; Greiner et al. 1999; Stock et al. 2011; Fernández-Martín et al. 2012).

7.2 Electron-scattering line wings

Strong emission lines in WR-type spectra show [...] extended line wings which can be attributed to line photons that are redistributed by scattering on free electrons in the wind. The strength of these wings is sensitive to the degree of wind inhomogeneities, the so-called clumping (see Section 4.2). The spectra of massive WN stars are typically consistent with a clumping density contrast of $D = 4 \dots 10$ (Hillier 1991; Hamann & Koesterke 1998; Hamann et al. 2006).

In the spectrum of the CS of Abell 48 these electron-

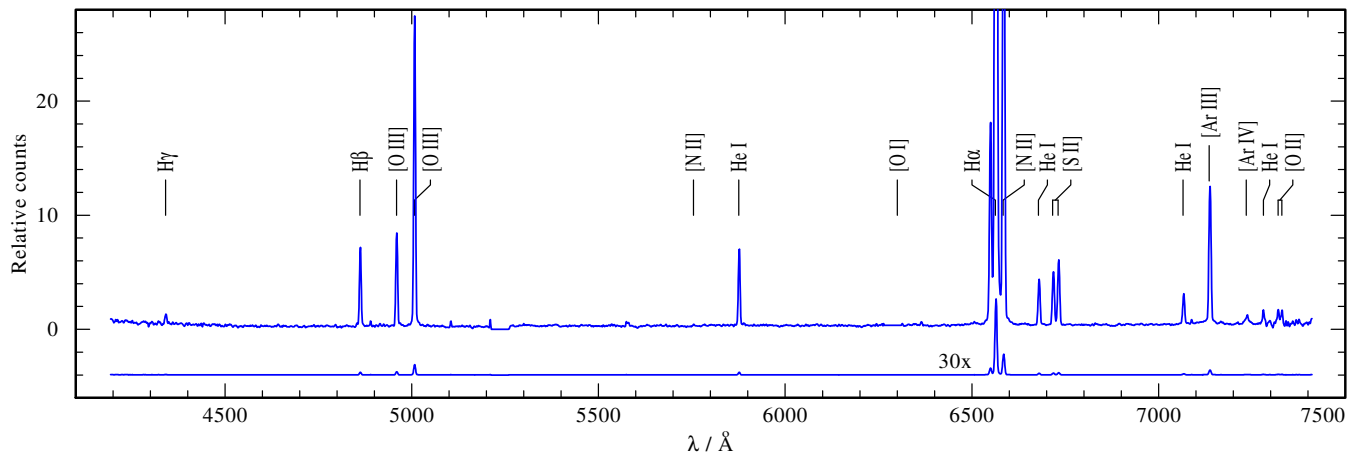


Figure 8. One-dimensional reduced spectrum of the nebula. Most of the detected strong emission lines of the nebula are marked. All detected and measured lines for the nebula are listed in Table 4. The lower spectrum is scaled by $1/30$ to show the relative intensities of strong lines.

scattering line wings are very weak and barely visible, while in contrast the massive WN models display significantly stronger wings.

However, the models which we have calculated for central star parameters, i.e. with $\log L/L_{\odot} = 3.7$ and $M = 0.6 M_{\odot}$ (cf. Section 5), show only weak electron-scattering line wings [...] with the same values for the clumping contrast as for massive WN stars, consistent with the observation. We consider this as an evidence for the low-mass nature of the CS of Abell 48.

7.3 Location and luminosity of the CS of Abell 48

The best fit to the SED of the CS of Abell 48 was achieved with a color excess $E_{B-V} = 2.10 \pm 0.05$ mag (which agrees well with $E_{B-V} = 2.15 \pm 0.01$ mag derived from the line ratios in the spectrum of the nebula; see Section 6.2), implying an extinction in the visual of $A_V \approx 7$ mag. The latter translates into $A_{K_s} \approx 0.8$ mag, if one adopts the extinction law from Rieke & Lebofsky (1985). These values should be compared with the full Galactic V and K_s -band extinctions in the direction of Abell 48, which according to Schlegel et al. (1998)⁵ are ≈ 34 and 4 mag, respectively. Thus, one can expect that Abell 48 is located at a factor of ~ 5 smaller distance, d , than the line-of-sight depth of the Galaxy of ≈ 20 kpc (e.g. Churchwell et al. 2009), i.e. at $d \approx 4$ kpc. Similar distance estimate ($d \approx 3.9$ kpc) could be derived if one assumes an average of 1.8 mag of visual extinction per kpc in the Galactic plane.

These distance estimates are supported by a study of the distribution of interstellar extinction towards $l \approx 29^\circ$, which shows that A_{K_s} grows from ≈ 0.3 to 1.0 mag between 2.5 and 4 kpc, then reaches a values of ≈ 1.5 mag at 6 kpc, and then abruptly increases to ≈ 2.5 mag between 6 and 7 kpc (Negueruela et al. 2011). Since A_{K_s} towards Abell 48 is ≈ 0.8 mag, one has that this object should be located in the Scutum-Centaurus arm at $d < 4$ kpc (see fig. 12 in Negueruela et al. 2011) and that its luminosity of $\log L/L_{\odot} \leq 4.3$

is much smaller than the lowest plausible luminosity for a massive WN star of $\log L/L_{\odot} \gtrsim 5.3$ (Hamann et al. 2006), but within the range of luminosities derived for CSPNe (e.g. Miller Bertolami & Althaus 2007). We adopt the typical luminosity of CSPNe of $L = 6000 L_{\odot}$ (see Section 5), which leads to a distance to Abell 48 of $d = 1.9$ kpc. Note that the luminosity of Abell 48 and its R_* and \dot{M} (given in Table 3) can be scaled to different distances as $\propto d^2$, $\propto d$, and $\propto d^{3/2}$, respectively (Schmutz et al. 1989).

Alternatively, if the CS of Abell 48 were a massive WN star, then it should be located well beyond the Sagittarius Arm. Indeed, if using the mean K_s -band absolute magnitude of massive WN5-6 stars from Crowther et al. (2006), $M_{K_s} = -4.41$ mag and the K_s -band extinction derived from the SED fitting and line ratios in the spectrum of the nebula, one gets a distance modulus of 15.94 mag, which translates into a distance of 15.4 kpc. An even larger distance would be derived, if one estimates A_{K_s} from the intrinsic $J - K_s$ color of WN5-6 stars of 0.18 mag given in Crowther et al. (2006). In this case, one gets $A_{K_s} = 0.66$ mag and $d = 16.4$ kpc. These two distance estimates imply that Abell 48 would be located either in the Perseus or the Outer Arm. This location, however, is in contradiction with the moderate extinction towards Abell 48 in view of the presence of an extinction wall at ≈ 6 kpc (e.g. Negueruela et al. 2011).

7.4 Abell 48 as a runaway

The short distance to Abell 48 is also supported by the detection of a significant proper motion for its CS: $\mu_{\alpha} \cos \delta = -13.3 \pm 4.8$ mas yr⁻¹ and $\mu_{\delta} = -14.8 \pm 4.8$ mas yr⁻¹ (Röser et al. 2010). To convert this proper motion and the radial velocity of Abell 48 (see Table 3) into the peculiar transverse and radial velocities, we used the Galactic constants $R_0 = 8.0$ kpc and $\Theta_0 = 240$ km s⁻¹ (Reid et al. 2009) and the solar peculiar motion $(U_{\odot}, V_{\odot}, W_{\odot}) = (11.1, 12.2, 7.3)$ km s⁻¹ (Schönrich et al. 2010). The derived velocity components and the total space velocity are given in Table 6 and imply that Abell 48 is a runaway system (e.g. Blaauw 1961). For the error calculation, only the errors of the proper motion and radial velocity measurements were considered. The

⁵ See also <http://irsa.ipac.caltech.edu/applications/DUST/>

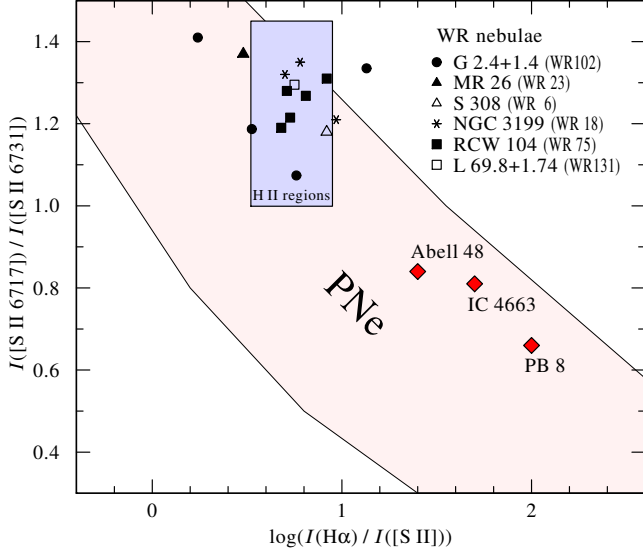


Figure 9. Diagnostic diagram $H\alpha/([S II] \lambda\lambda 6717, 6731)$ intensity ratio versus $[S II] \lambda\lambda 6717/6731$ ratio as a measure of electron density versus excitation for gaseous nebulae. Shown are the locations for H II regions as well as the positions of WR nebulae from (Esteban et al. 1992). Most PNe lie on the indicated strip from (Riesgo-Tirado & López 2002). Also labeled are the positions of the [WN] and [WN/WC] stars Abell 48, IC 4663, and PB 8 to demonstrate their CSPNe status.

Table 6. Abell 48: Peculiar transverse (in Galactic coordinates), radial and total space velocities, and height over the Galactic plane for different adopted distances.

d [kpc]	v_l [km s ⁻¹]	v_b [km s ⁻¹]	v_r [km s ⁻¹]	v_{pec} [km s ⁻¹]	$d \sin b$ [pc]
1.9	-149 ± 43	53 ± 43	37 ± 4	162 ± 42	15
4.0	-296 ± 91	104 ± 91	-8 ± 4	314 ± 91	32
15.4	-970 ± 350	378 ± 350	74 ± 4	1043 ± 349	122

peculiar radial velocity of Abell 48 contributes only slightly to its total space velocity, v_{pec} (Table 6). These estimates show that the larger d the larger v_{pec} and correspondingly the lower the likelihood that the CS of Abell 48 can be accelerated to such high velocity. Consequently, one can conclude that the short distance to Abell 48 is more likely.

The runaway status of Abell 48 is consistent with the orientation of its peculiar velocity with respect to the Galactic plane. Fig. 10 shows the *MSX* 8.3 μ m image of a $2^\circ \times 2^\circ$ region of the Galactic plane (centered at $l = 29^\circ, b = 0^\circ.5$). One can see that Abell 48 is moving in the “correct” direction, i.e. away from the Galactic plane. On the other hand, the large margin of error in v_b leaves the possibility that Abell 48 is moving almost parallel to the Galactic plane, which in turn is consistent with the small height above the Galactic plane (cf. Table 6).

7.5 Classification

Based on the arguments above we conclude that Abell 48 is a PN with a low-mass central star.

The abundance pattern, that our spectral analysis revealed, corresponds to a WN-type composition, where is he-

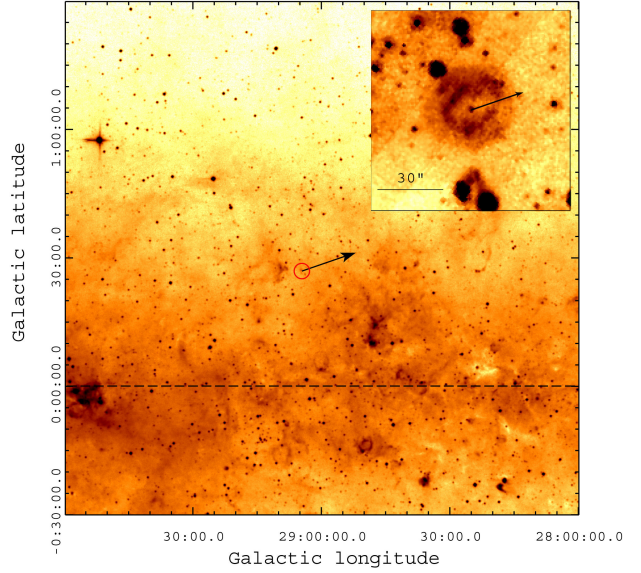


Figure 10. $2^\circ \times 2^\circ$ *MSX* 8.3 μ m image of the Galactic plane (shown by a dashed line) centered at $l = 29^\circ, b = 0^\circ.5$, with the position of Abell 48 indicated by a circle. The inset shows the *IRAC* 8 μ m image of Abell 48. The arrows on both images show the direction of motion of Abell 48. The orientation of the images is the same.

Table 7. Measured line ratios from the spectrum of the CS of Abell 48 for spectral subtype classification.

line ratio	peak/continuum
N v 4604 / N III 4640	2.0
C IV 5808 / He II 5411	0.7
C IV 5808 / He I 5878	1.7

lium dominates, nitrogen is enhanced and the carbon and oxygen abundances are roughly solar. Therefore, we suggest to assign Abell 48 to the [WN] class, becoming thus the second known member of this spectral class after IC 4663 (Miszalski et al. 2012).

To determine the detailed subtype of Abell 48, we apply the 3D classification scheme by Smith et al. (1996). The measured line ratios (see Table 2 and 7) suggest that the star belongs to the [WN 5] subtype.

In this connection, we note that none of the massive WNE stars possess a compact circumstellar nebula (Gvaramadze et al. 2009, 2010a, and references therein), which provides one more evidence in support of the PN status of Abell 48.

7.6 Evolutionary status

Spectroscopically, Abell 48 with its strong helium and nitrogen emission lines belongs clearly to the [WN] class. However, Abell 48 seems to be different in some respect from the other [WN] star IC 4663. While Miszalski et al. (2012) could not find any residual hydrogen in IC 4663, the presence of some hydrogen is indicated by our optical spectrum of the CS of Abell 48. Such residual hydrogen would rule out a merger scenario with a sequence He-WD + He-WD \rightarrow

[WN] \rightarrow O(He) as proposed by Reindl et al. (in prep.) for the O(He) and [WN] stars. Moreover, if the nebula of Abell 48 has been ejected during the merging process it would be hydrogen-deficient, contrary to the observation. Thus, there must exist different evolutionary channels for the formation of these two [WN] stars.

For the [WN/WC] star PB 8 Miller Bertolami et al. (2011) suggested a diffusion-induced nova (DIN) of a low-mass ($M \lesssim 0.6 M_{\odot}$) post-AGB object as the origin of such stars. Among the models calculated for the different scenarios of the DIN there is one which includes overshooting in the convective zone generated during the CNO-flash, which has abundances that are very similar to those that we found for Abell 48. The surface abundances of the model are H:He:C:N:O=22:73:0.66:3.8:0.1 per cent by mass, that is close to our results of H:He:C:N:O=10:85:0.3:5:0.6 for the wind of Abell 48.

The nebula abundance ratio $N/O = 0.25$ is below the sharp limit of $N/O > 0.8$ that Kaler & Jacoby (1989) deduced for N-enriched PNe, which are supposed to indicate hot bottom burning in more massive AGB-stars with $M_{\text{core}} > 0.8 M_{\odot}$. The low core mass of Abell 48 would be in line with the models by Miller Bertolami et al. (2011).

However, the stellar evolutionary models by Miller Bertolami et al. (2011) assume a low-metallicity ($Z = 0.001$) progenitor, which is at least for the CS of PB 8 not the case, as we inferred solar-like iron-group abundances from the UV spectra of this object. For the CS of Abell 48 we could not determine any iron-group abundances, but the metallicity of the nebula is roughly solar (cf. Table 5).

Further problems for this scenario are posed by the involved timescales. Assuming a PN radius of 0.2 pc as deduced in Section 6.1 and a typical expansion velocity of 30 km s^{-1} , the nebula age is only 6500 yr. This is far too short compared to the evolutionary time since the ejection of the nebula at the AGB ($10^6 - 10^7$ yr, Miller Bertolami et al. 2011), especially since this scenario works only for low stellar masses $M \lesssim 0.6 M_{\odot}$.

ACKNOWLEDGMENTS

All SAAO and SALT co-authors acknowledge the support from the National Research Foundation (NRF) of South Africa. We would also like to thank Martin Wendt for fruitful discussions of χ^2 -fitting techniques.

This work has made use of the NASA/IPAC Infrared Science Archive, which is operated by the Jet Propulsion Laboratory, California Institute of Technology, under contract with the National Aeronautics and Space Administration, the SIMBAD database and the VizieR catalogue access tool, both operated at CDS, Strasbourg, France.

REFERENCES

- Abell G. O., 1955, *PASP*, 67, 258
 Abell G. O., 1966, *ApJ*, 144, 259
 Acker A., Marcout J., Ochsenbein F., Stenholm B., Tytenda R., Schohn C., 1992, *The Strasbourg-ESO Catalogue of Galactic Planetary Nebulae. Parts I, II*.
 Asplund M., Grevesse N., Sauval A. J., Scott P., 2009, *ARA&A*, 47, 481
 Benjamin R. A. et al., 2003, *PASP*, 115, 953
 Blaauw A., 1961, *Bull. Astron. Inst. Netherlands*, 15, 265
 Bojicic I. S., Frew D. J., Parker Q. A., Stupar M., Wachter S., DePew K., 2012, *arXiv:1212.5382*
 Buckley D. A. H., Swart G. P., Meiring J. G., 2006, *SPIE*, 6267
 Burgh E. B., Nordsieck K. H., Kobulnicky H. A., Williams T. B., O'Donoghue D., Smith M. P., Percival J. W., 2003, *SPIE*, 4841, 1463
 Carey S. J. et al., 2009, *PASP*, 121, 76
 Churchwell E. et al., 2009, *PASP*, 121, 213
 Cohen M., Megeath S. T., Hammersley P. L., Martín-Luis F., Stauffer J., 2003, *AJ*, 125, 2645
 Condon J. J., Cotton W. D., Greisen E. W., Yin Q. F., Perley R. A., Taylor G. B., Broderick J. J., 1998, *AJ*, 115, 1693
 Condon J. J., Kaplan D. L., 1998, *ApJS*, 117, 361
 Crawford S. M. et al., 2010, *SPIE*, 7737, 54
 Crowther P. A., Hadfield L. J., Clark J. S., Negueruela I., Vacca W. D., 2006, *MNRAS*, 372, 1407
 Cutri R. M. et al., 2003, *VizieR Online Data Catalog*, 2246, 0
 DENIS Consortium, 2005, *VizieR Online Data Catalog*, 2263, 0
 DePew K., Parker Q. A., Miszalski B., De Marco O., Frew D. J., Acker A., Kovacevic A. V., Sharp R. G., 2011, *MNRAS*, 414, 2812
 Esteban C., Vilchez J. M., Smith L. J., 1994, *AJ*, 107, 1041
 Esteban C., Vilchez J. M., Smith L. J., Clegg R. E. S., 1992, *A&A*, 259, 629
 Fazio G. G. et al., 2004, *ApJS*, 154, 10
 Fernández-Martín A., Martín-Gordón D., Vilchez J. M., Pérez Montero E., Riera A., Sánchez S. F., 2012, *A&A*, 541, A119
 Fitzpatrick E. L., 1999, *PASP*, 111, 63
 Frew D. J., Parker Q. A., 2010, *PASA*, 27, 129
 Garnett D. R., Chu Y.-H., 1994, *PASP*, 106, 626
 Górny S. K., Tytenda R., 2000, *A&A*, 362, 1008
 Gräfener G., Hamann W.-R., 2005, *A&A*, 432, 633
 Gräfener G., Koesterke L., Hamann W.-R., 2002, *A&A*, 387, 244
 Greiner J., Tovmassian G., Komossa S., Rosado M., Arrieta A., 1999, *A&A*, 347, 556
 Gvaramadze V. V., Chené A.-N., Kniazev A. Y., Schnurr O., 2011, *arXiv:1110.0126*
 Gvaramadze V. V. et al., 2009, *MNRAS*, 400, 524
 Gvaramadze V. V., Kniazev A. Y., Fabrika S., 2010a, *MNRAS*, 405, 1047
 Gvaramadze V. V., Kniazev A. Y., Fabrika S., Sholukhova O., Berdnikov L. N., Cherepashchuk A. M., Zharova A. V., 2010b, *MNRAS*, 405, 520
 Gvaramadze V. V., Kniazev A. Y., Hamann W.-R., Berdnikov L. N., Fabrika S., Valeev A. F., 2010c, *MNRAS*, 403, 760
 Gvaramadze V. V. et al., 2012, *MNRAS*, 421, 3325
 Hamann W.-R., Gräfener G., 2004, *A&A*, 427, 697
 Hamann W.-R., Gräfener G., Liermann A., 2006, *A&A*, 457, 1015
 Hamann W.-R., Koesterke L., 1998, *A&A*, 335, 1003

- Helfand D. J., Becker R. H., White R. L., Fallon A., Tuttle S., 2006, *AJ*, 131, 2525
- Hillier D. J., 1991, *A&A*, 247, 455
- Holberg J. B., Bergeron P., 2006, *AJ*, 132, 1221
- Kaler J. B., Jacoby G. H., 1989, *ApJ*, 345, 871
- Kniazhev A. Y., Grebel E. K., Pustilnik S. A., Pramskij A. G., Zucker D. B., 2005, *AJ*, 130, 1558
- Kniazhev A. Y., Pustilnik S. A., Grebel E. K., Lee H., Pramskij A. G., 2004, *ApJS*, 153, 429
- Kniazhev A. Y., Pustilnik S. A., Zucker D. B., 2008a, *MNRAS*, 384, 1045
- Kniazhev A. Y. et al., 2008b, *MNRAS*, 388, 1667
- Kobulnicky H. A., Nordsieck K. H., Burgh E. B., Smith M. P., Percival J. W., Williams T. B., O'Donoghue D., 2003, *SPIE*, 4841, 1634
- Liermann A., Hamann W.-R., Oskinova L. M., Todt H., Butler K., 2010, *A&A*, 524, A82
- McLean B. J., Greene G. R., Lattanzi M. G., Pirenne B., 2000, in *Astronomical Society of the Pacific Conference Series*, Vol. 216, *Astronomical Data Analysis Software and Systems IX*, Manset N., Veillet C., Crabtree D., eds., p. 145
- Miller Bertolami M. M., Althaus L. G., 2007, *MNRAS*, 380, 763
- Miller Bertolami M. M., Althaus L. G., Olano C., Jiménez N., 2011, *MNRAS*, 415, 1396
- Miszalski B., Crowther P. A., De Marco O., Köppen J., Moffat A. F. J., Acker A., Hillwig T. C., 2012, *MNRAS*, 423, 934
- Negueruela I., González-Fernández C., Marco A., Clark J. S., 2011, *A&A*, 528, A59
- O'Donoghue D., et al., 2006, *MNRAS*, 372, 151
- Phillips J. P., Ramos-Larios G., 2008, *MNRAS*, 383, 1029
- Price S. D., Egan M. P., Carey S. J., Mizuno D. R., Kuchar T. A., 2001, *AJ*, 121, 2819
- Reid M. J., Menten K. M., Zheng X. W., Brunthaler A., Xu Y., 2009, *ApJ*, 705, 1548
- Rieke G. H., Lebofsky M. J., 1985, *ApJ*, 288, 618
- Rieke G. H. et al., 2004, *ApJS*, 154, 25
- Riesgo-Tirado H., López J. A., 2002, in *Revista Mexicana de Astronomía y Astrofísica Conference Series*, Henney W. J., Franco J., Martos M., eds., Vol. 12, pp. 174–174
- Röser S., Demleitner M., Schilbach E., 2010, *AJ*, 139, 2440
- Sanduleak N., 1976, *Publications of the Warner & Swasey Observatory*, 2, 57
- Schlegel D. J., Finkbeiner D. P., Davis M., 1998, *ApJ*, 500, 525
- Schmutz W., Hamann W.-R., Wessolowski U., 1989, *A&A*, 210, 236
- Schönberner D., Jacob R., Steffen M., Perinotto M., Corradi R. L. M., Acker A., 2005, *A&A*, 431, 963
- Schönrich R., Binney J., Dehnen W., 2010, *MNRAS*, 403, 1829
- Smith L. F., Shara M. M., Moffat A. F. J., 1996, *MNRAS*, 281, 163
- Stock D. J., Barlow M. J., Wesson R., 2011, *MNRAS*, 418, 2532
- Stringfellow G. S., Gvaramadze V. V., Beletsky Y., Kniazhev A. Y., 2011, *arXiv:1112.2686*
- Stringfellow G. S., Gvaramadze V. V., Beletsky Y., Kniazhev A. Y., 2012, in *IAU Symposium*, Richards M. T., Hubeny I., eds., Vol. 282, p. 267
- Todt H., Peña M., Hamann W.-R., Gräfener G., 2010a, *A&A*, 515, A83
- Todt H., Peña M., Hamann W.-R., Gräfener G., 2010b, in *American Institute of Physics Conference Series*, Werner K., Rauch T., eds., Vol. 1273, pp. 219–224
- Torres-Peimbert S., Arrieta A., Georgiev L., Richer M., 2009, in *Revista Mexicana de Astronomía y Astrofísica Conference Series*, Vol. 35, pp. 39–45
- Wachter S., Mauerhan J. C., Van Dyk S. D., Hoard D. W., Kafka S., Morris P. W., 2010, *AJ*, 139, 2330
- Werner K., Heber U., 1991, *A&A*, 247, 476
- Wright E. L. et al., 2010, *AJ*, 140, 1868
- Zasov A. V., Kniazhev A. Y., Pustilnik S. A., Pramsky A. G., Burenkov A. N., Ugryumov A. V., Martin J.-M., 2000, *A&AS*, 144, 429